Energy &
Environmental
Science

PAPER

View Article Online
View Journal

Published on 18 February 2022. Downloaded by University of Central Florida on 4/7/2022 4:15:53 PM.

Check for updates

Cite this: DOI: 10.1039/d1ee03972e

Surface oxygenation induced strong interaction between Pd catalyst and functional support for zinc–air batteries†

Wei Zhang,[ab] Jinfa Chang,[a] Guanzhi Wang,[ab] Zhao Li,[ab] Maoyu Wang,[c] Yuanmin Zhu,[de] Boyang Li,[f] Hua Zhou,[g] Guofeng Wang,[f] Meng Gu,[e] Zhenxing Feng*[c] and Yang Yang*[abhi]

Received 24th October 2021,
Accepted 18th February 2022

DOI: 10.1039/d1ee03972e

rsc.li/ees

Employing the strong metal-support interaction (SMSI) effect for promoting the catalyst's activity toward the oxygen reduction reaction (ORR) is promising due to the electronic structure optimization and high utilization efficiency of platinum group metal (PGM) catalysts. Metal oxides as alternative supports for PGMs facilitate intrinsic activity and improve durability as compared to conventional carbon supports. However, the restricted mass and electron transfer at the metal/support interface need to be addressed. Herein, to strengthen the interaction at the metal/support interfaces and improve the utilization efficiency of PGM, an ultralow loading of Pd was embedded in a surface-oxygenated PdNiMnO porous film. The Mn-doping was designed to promote surface oxygenation using a facile anodization process that created sufficiently exposed interfaces between Pd and the support, strengthening the SMSI effects at the Pd/oxygenated support interface for enhancing ORR performance. Furthermore, the Ni-containing oxygenated catalyst served as both the active component for the oxygen evolution reaction (OER) and the functional support for stabilizing Pd, making PdNiMnO a bifunctional catalyst for zinc–air flow batteries (ZAFB). As a proof-of-concept, the ZAFB (PdNiMnO) shows a maximal power density of 211.6 mW cm^{-2} and outstanding cycling stability for over 2000 h with a minimal voltage gap of 0.69 V at a current density of 10 mA cm^{-2}, superior to the state-of-the-art catalysts.

Broader context

Employing the strong metal-support interaction (SMSI) effect for promoting the catalyst's activity toward the oxygen reduction reaction (ORR) is promising due to the electronic structure optimization and high utilization efficiency of platinum group metal (PGM) catalysts. We have proposed a new strategy to strengthen the SMSI effects in a rationally designed materials system consisting of trace amounts of Pd embedded inside functionally oxygenated supports (FOS). We have proved the significant role of FOS in regulating the electronic structure of Pd active sites and optimizing the adsorption and cleavage of O_2 during ORR. We have also verified the role of FOS in serving as the active phase for the oxygen evolution reaction (OER), which makes the proposed materials bifunctional for Zn–air batteries (ZAB). The proposed concept of FOS can be applied to broader fields where the SMSI plays a crucial role in realizing performance improvement.

Introduction

Nowadays, growing markets for consumer electronics and electrical cars spur the development of energy conversion and storage technologies with high efficiency and sustainability.[1,2] Thus far, enormous efforts and investments have been focused on the emerging Zn–air batteries (ZAB) due to their superior theoretical energy density as compared to Li-ion batteries (LIB).[3,4] In addition, their low cost, zero-emission, and less toxic aqueous electrolytes largely reduce safety and environmental concerns.[3] The discharging performance of ZAB is markedly dependent on the oxygen reduction reaction (ORR) at the cathode, during which O_2 receives electrons and is

---

[a] *NanoScience Technology Center, University of Central Florida, Orlando, FL 32826, USA. E-mail: Yang.Yang@ucf.edu*
[b] *Department of Materials Science and Engineering, University of Central Florida, Orlando, FL 32826, USA*
[c] *School of Chemical, Biological, and Environmental Engineering, Oregon State University, Corvallis, OR 97331, USA. E-mail: zhenxing.feng@oregonstate.edu*
[d] *Department of Materials Science and Engineering, Dongguan University of Technology, Dongguan 523808, China*
[e] *Department of Materials Science and Engineering, Southern University of Science and Technology, Shenzhen 518055, China*
[f] *Department of Mechanical Engineering and Materials Science, University of Pittsburgh, Pittsburgh, PA 15261, USA*
[g] *X-Ray Science Division, Argonne National Laboratory, Lemont, IL 60439, USA*
[h] *Renewable Energy and Chemical Transformation Cluster, University of Central Florida, Orlando, FL 32826, USA*
[i] *Department of Chemistry, University of Central Florida, Orlando, FL 32826, USA*

† Electronic supplementary information (ESI) available. See DOI: 10.1039/d1ee03972e

Published on 18 February 2022. Downloaded by University of Central Florida on 4/7/2022 4:15:53 PM.

reduced to the hydroxyl group in an alkaline environment, and *vice versa* for the oxygen evolution reaction (OER), shaping the charging behavior. However, the performance of ZAB is significantly inhibited by the sluggish 4-electron transfer process and large overpotentials at the cathode caused by the barriers for surface electrochemical processes on the catalysts including O_2 adsorption/desorption, O–O cleavage/association as well as interaction with oxygen-containing intermediates.[5,6] Thus, developing a highly efficient bifunctional catalyst for the cathode reaction is of vital importance. It is widely accepted that platinum group metals (PGMs) are essentially the most efficient catalysts for ORR/OER compared to the transition metals due to their unique electronic structures interacting with oxygen molecules and intermediate species.[7,8] Nevertheless, the high cost of PGM-based catalysts significantly hinders the rapid growth of the ZAB market in the field of renewable energy.

To overcome the cost barrier, extensive efforts have been devoted to the exploration of various strategies to improve the performance of low-PGM and non-PGM catalysts in order to pursue the increasing demands for highly efficient energy storage and conversion systems. For instance, surface/interface engineering has been demonstrated to be an efficient strategy for tunning the size, shape, and surface morphology of the catalysts to accommodate less PGM at the interfaces.[9] Alloying PGM with transition metals (Fe, Co, Ni) can sufficiently expose the active sites and modify the electronic structures of PGM.[10–12] Engineering the interface between metal and oxides can promote interfacial electron/mass (O_2, intermediate species, and products) transfer.[13,14] In addition, transition metal oxides (*e.g.*, MnO_x, CoO_x, FeO_x) with multiple chemical states may show unique adsorption/interaction with oxygen, which is, however, still inferior to the PGM-based ORR catalysts due to the poor electron transfer across the interfaces.[15,16] Besides, employing strong metal-support interaction (SMSI) is a promising method for tuning the electronic structures at the materials' interfaces, which is responsible for the preeminent catalytic activities.[17,18] For example, improved ORR activities were achieved on Pt/NbO_x interfaces in the $Pt/NbO_x/C$ system by shortening the Pt–Pt bond distance and constructing electron-deficient low-coordination Pt sites.[17] Whereas, a reverse trend was observed for electron donation from the NbO_2 layer to the Pt layer, leading to excessive electrons on Pt that tuned the interaction between chemisorbed species and Pt sites.[19] Thus, the degree of oxygen incorporation, morphology, as well as the electronic structure at the metal/support interface together determine the SMSI effect and thus the ORR performance. However, most of the oxide supports (*e.g.*, NbO_x) designed for SMSI are inert to both the ORR and OER, thus limiting their practical applications in ZAB. Therefore, we suggest that functionally oxygenated supports (FOS) with maximal exposure area of PGM and active components for OER will be an ideal option for applying the SMSI effect in ZAB, which will ensure the improved electron and mass transfer across the interfaces.

When applying the SMSI effect in designing novel PGM-based catalysts, the FOS possesses many advantages over conventional supports because of their ability to modulate the electronic structure of active sites, which further optimizes the adsorption and cleavage of O_2.[20] In addition, compared with PGM alloys and traditional carbon-based PGM, which may undergo severe PGM dissolution, agglomeration, and Ostwald ripening, *etc.*, during the long period of operation due to leaching of transition group metal and carbon corrsion,[21] the preeminent features of carbon-free FOS for preventing PGM from deactivation based on strong SMSI effect during the operation of ZAB make them promising candidates to replace conventional supports.[22,23] Furthermore, the FOS can serve as secondary adsorption sites for reaction intermediates, which play a crucial role in lowering the reaction energy barrier.[22,24] However, the traditional synthesis routes (*e.g.*, high-temperature annealing and vacuum deposition) of FOS can only produce a limited number of catalyst/support interfaces,[18,25] which severely lowers the surface active sites and thus hinders the mass transfer process.[17,26] Besides, the poor electron transfer across the interfaces obstructs the delivery of the intrinsic catalytic activity in ZAB.[27] Thus, it is non-trivial to develop an efficient approach to FOS with sufficiently exposed catalyst/support interfaces for favoring mass and electron transfer by the SMSI effect.

Pd-based catalysts are promising alternatives to Pt-based materials for the ORR due to their similar catalytic activity but higher abundance than Pt.[28–30] However, modulating the electronic structure of Pd to optimize surface reaction kinetics towards the ORR is still required.[31] To this end, we suggest building up a porous film (PF) of the Pd/FOS catalyst with a rationally designed oxygenated support for the boosted SMSI effect. The porous structure of Pd/FOS can effectively expose active sites on the surface and strengthen the interaction between Pd and FOS, thus ensuring high activity throughout the porous network. Our prior studies proved that the anodization treatment is a facile approach to the surface oxygenated Ni-based porous materials for electrocatalytic reactions,[32] which was adopted in this work for the synthesis of the proposed Pd/FOS-PF, since Pd could be embedded in the oxygenated Ni support (FOS). We also doped Mn into Ni-based PF to promote the formation of surface oxygenation and tune the valence state of metals because of the various oxidation states of Mn^{x+} (x = 2, 3, 4, 6,7).[33] Furthermore, the surface oxygenated Mn-doped Ni porous film (denoted as NiMnO-PF, which represents the general chemical composition instead of the exact stoichiometry), can serve as FOS for the immobilization of Pd catalysts as well as an active component for the OER in ZAB. The novel surface oxygenation strategy ensures the seamless interaction between countless Pd/FOS interfaces as compared with the conventional metal-support system. This strengthened SMSI effect will benefit the mass and electron transfer as well as stabilize the exposed Pd active sites for long-term utilization in ZAB.[20,34]

Herein, to verify the aforementioned concept of Pd/FOS-PF in promoting ZAB performance throughout the SMSI effect, we electrodeposited PdNiMn film with ultralow Pd loading as precursor materials, which were then anodized to form oxygenated PdNiMnO-PF. As a result, the oxygenation of Ni and Pd was achieved in the PdNiMnO-PF rather than the control

Published on 18 February 2022. Downloaded by University of Central Florida on 4/7/2022 4:15:53 PM.

catalyst of PdNiO-PF without Mn because of the promoted surface oxygenation by Mn-doping. Note that "PdNiMnO" represents metallic Pd, PdO as well as FOS instead of exact stoichiometry. Therefore, the strengthened interaction between Pd and the oxygenated NiMnO-PF support is responsible for the boosted ORR activity due to the accelerated charge transfer across the Pd/NiMnO interfaces. Also, the formed oxygenated phase around Pd active sites may act as secondary adsorption sites for lowering the reaction energy barrier.[24,35] On the other hand, the NiMnO is the active component for OER, enabling the PdNiMnO-PF bifunctional ORR/OER activities for ZAB applications.[36,37] As a proof-of-concept, Zn–air flow batteries (ZAFB) assembled with PdNiMnO-PF as the cathode delivered a maximum power density of 211.6 mW cm^{-2} and ultrahigh cycling stability for 2000 h, superior to state-of-the-art catalysts.

Results and discussion

A bottom-up electrodeposition method (see the ESI† for experimental details) was employed to synthesize the PdNiMn film, followed by a top-down anodization treatment to fabricate PdNiMnO-PF consisting of the well-pronounced surface oxygenation of metals. The porous structure of PdNiMnO-PF, showing an interconnected network, not only enables the easy access of the electrolyte to Pd/NiMnO for the electrocatalysis of O_2 but also facilitates the electron transfer across the Pd/NiMnO interface due to the strong SMSI effect. Scanning electron microscope (SEM) images (Fig. 1a–c) display an interconnected porous structure of PdNiMnO-PF with pore size in the range of 30–100 nm. We also prepared PdNiO porous film (denoted as PdNiO-PF) as a control catalyst to study the role of Mn in surface oxygenation (Fig. S1, ESI†). The exposed electrochemical active surface areas (ECSA) of PdNiMnO-PF and PdNiO-PF for electrochemical reactions were estimated by calculating the electrical double layer capacitance (C_{dl}, Fig. S2, ESI†), similar to C_{dl} measured from electrochemical impedance spectroscopy (EIS) at open circuit potential (OCP)[38] (Fig. S3, ESI†). Note that the non-rectangular shape of CV curves is attributed to non-ideal capacitor behavior due to non-uniform pore structure and current distribution.[39] The PdNiMnO-PF has a higher ECSA

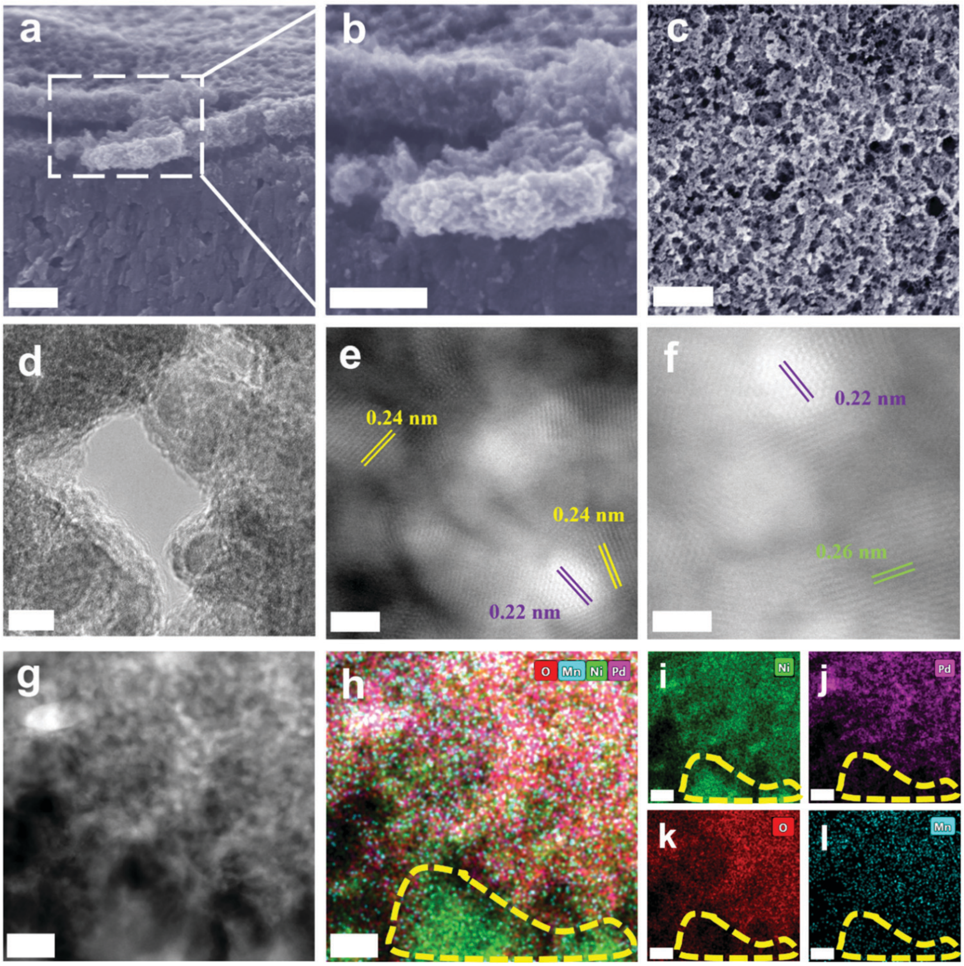

Fig. 1 Microscopic characterizations of PdNiMnO-PF. (a–c) Cross-sectional, enlarged, and top-view SEM images, respectively. (d) HRTEM and (e and f) STEM-HAADF images. Lattice fringes of Pd, PdO, and NiO are marked with purple, green, and yellow, respectively. (g) HAADF image, (h) the corresponding overlapped EDS elemental mapping, and the corresponding individual EDS elemental mapping for (i) Ni, (j) Pd, (k) O, and (l) Mn, respectively. Scale bars: (a–c) 200 nm, (d) 5 nm, (e and f) 2 nm, and (g–i) 20 nm.

Published on 18 February 2022. Downloaded by University of Central Florida on 4/7/2022 4:15:53 PM.

than PdNiO-PF, opening more active surface sites for the catalytic reactions.

High-resolution transmission electron microscopy and high-angle annular dark-field scanning transmission electron microscopy (HAADF-STEM) images (Fig. 1d–f) show the porous and well-crystallized structure of PdNiMnO-PF, suggesting the presence of a large number of small boundaries between Pd and NiMnO, which ensures a large number of exposed Pd/NiMnO interfaces, which can maintain the intimate electron transfer across the interfaces between Pd and the oxygenated support. The *d*-spacings of 0.24 nm and 0.26 nm were identified, corresponding to the lattice planes of NiO (111)[40] and PdO (101),[41] respectively, confirming the coexistence of the surface oxygenated metals. Also, the metallic Pd active sites with a *d*-spacing of 0.22 nm, corresponding to the Pd (111) plane, were identified around the neighboring oxygenated phase. The HAADF image (Fig. 1g) and corresponding energy-dispersive X-ray spectroscopy (EDS) elemental mapping (Fig. 1h–l) of PdNiMnO-PF show the distribution of Pd, Ni, Mn, and O over the porous structure. The circled area (untreated region underneath the catalyst layer) dominantly consists of Ni and other minor elements. In contrast, the distribution of Pd, Ni, Mn, and O outside the circled area is highly matched, suggesting that the surface oxygenation is promoted probably due to the improved lattice oxygen diffusion induced by the incorporation of multi-valence Mn.[33,42] Moreover, the cross-sectional HAADF image (Fig. S4a, ESI†) and corresponding EDS elemental mapping (Fig. S4b–f, ESI†) of PdNiMnO-PF show the overall element distributions across the catalyst. An apparent phase boundary between the catalyst layer (PdNiMnO-PF) and compact PdNiMn substrate (untreated region, used as the conducting current collector in ZAB) was observed. The increased relative concentration of Pd in the surface porous structure of the catalyst layer implies the sufficiently exposed Pd active sites and morphology reconstruction by anodization. Note that the PdNiMnO-PF directly grew underneath the PdNiMn substrate, forming a seamless interface that ensures high conductivity throughout the catalyst. The electron microscopy characterizations prove the successful fabrication of PdNiMnO-PF *via* one-pot electrodeposition coupled with a top–down anodization process.

To further probe the structural characteristics of the catalysts, X-ray diffraction (XRD, Fig. S5, ESI†) was employed to study the phase compositions of PdNiMnO-PF and PdNiO-PF. The PdNiMn substrates underneath the porous films of PdNiMnO-PF and PdNiO-PF were identified at 44.5°, 51.9°, and 76.5°, corresponding to Ni (111), (200), and (220), respectively (JCPDS: 1-1258). Note that the peaks for oxygenated Ni and Mn are absent in the diffraction pattern of PdNiMnO-PF because of the low content of the catalyst layer formed on the top surface of the materials, likewise for the PdNiO-PF. X-Ray fluorescence was used to quantify the bulk elemental information across the whole film. The atomic contents of Ni, Pd, and Mn were 99.25 at%, 0.41 at%, and 0.33 at%, respectively, for the PdNiMnO-PF, which are similar to those for the PdNiO-PF (Table S1, ESI†). Moreover, an ultralow loading of Pd in the PdNiMnO-PF was calculated to be 0.016 ± 0.008 mg cm^{-2} (Table S2, ESI†), remarkably reducing the cost of the catalysts used in the energy devices.

X-Ray photoelectron spectroscopy (XPS) was utilized to acquire the surface chemical states of PdNiMnO-PF and PdNiO-PF. The XPS Ni 2p spectra (Fig. 2a) show the presence of Ni^0 (852.8 and 870.2 eV) and oxygenated Ni (855.9 and 873.9 eV) for PdNiMnO-PF, and Ni^0 (852.6 and 870.0 eV), as well as oxygenated Ni (855.8 and 873.8 eV) for PdNiO-PF; the positive binding energy (BE) shift of ~0.1 eV for oxygenated Ni in PdNiMnO as compared to PdNiO, indicates the electron-donating nature of the oxygenated support.[43,44] The XPS O 1s spectra (Fig. 2b) show the lattice oxygen (M–O) peak at the BE of 529.9 eV for PdNiMnO-PF, which was negatively shifted by ~0.22 eV for PdNiO-PF (529.7 eV), implying the regulated electron-donating ability of lattice oxygen by Mn-doping. The BE of 531.7 and 533.4 eV for both PdNiMnO-PF and PdNiO-PF are attributed to the hydroxyl groups and water, respectively.[44] These hydroxyl groups may promote the desorption/removal of oxygen-containing intermediates, facilitating the reaction kinetics.[20,30] More importantly, a negative BE shift of ~0.32 eV for Pd^0 (Fig. 2c) was identified in the PdNiMnO-PF (335.1 and 340.4 eV) as compared with PdNiO-PF (335.4 and 340.7 eV), indicating the modified electron-withdrawing ability of Pd^0 by forming the oxygenated surface. Also, the BE assigned to Pd^{2+} is negatively shifted in the PdNiMnO-PF (335.8 and 341 eV) compared to PdNiO-PF (336.3 and 341.6 eV), suggesting the electron redistribution at the Pd/support interface.[45] It is also noteworthy that a higher concentration of Pd^{2+} was detected in the PdNiMnO-PF (39.4%) as compared to PdNiO-PF (16.7%), confirming the promoted formation of the oxygenated catalyst surface by Mn-doping. The notable electron transfer from the oxygenated catalyst surface to Pd observed in the PdNiMnO-PF indicates the tailored electronic structure at the Pd/support interface,[17,46] which may facilitate the reaction kinetics and O–O bond cleavage.[30] Based on the XPS characterization and analysis, the oxygenated catalyst around Pd may behave as secondary adsorption sites for oxygen-containing intermediates (*e.g.*, *OOH, *OH, and *O), thus lowering the reaction barrier.[24,35] However, we could not detect Mn 2p XPS signal due to the overlapped binding energy range with Ni LMM Auger peak (Fig. S6, ESI†),[47] suggesting the low doping content of Mn.[33] Ultraviolet photoelectron spectroscopy (UPS, Fig. S7, ESI†) was used to estimate the work function (WF) of the catalysts. A smaller WF of PdNiMnO-PF (4.7 eV) was obtained as compared to PdNiO-PF (5.24 eV), indicating the higher mobility and a lower hurdle for electrons to participate in the surface reactions.[48,49] Meanwhile, Raman spectroscopy (Fig. 2d) was employed to probe the oxygenated phase and identify the degree of surface oxygenation. A Raman peak centered at 508 cm^{-1} assigned to the Ni–O stretching vibration mode was observed in both PdNiMnO-PF and PdNiO-PF, further confirming the formation of oxygenated Ni in the porous films.[50] Compared with PdNiO-PF, the PdNiMnO-PF displayed more pronounced Pd–O vibration modes of E_g (431 cm^{-1}) and B_{1g} (634 cm^{-1}), indicating the higher amount of surface oxygenated Pd formed in the PdNiMnO-PF than

This journal is © The Royal Society of Chemistry 2022

Published on 18 February 2022. Downloaded by University of Central Florida on 4/7/2022 4:15:53 PM.

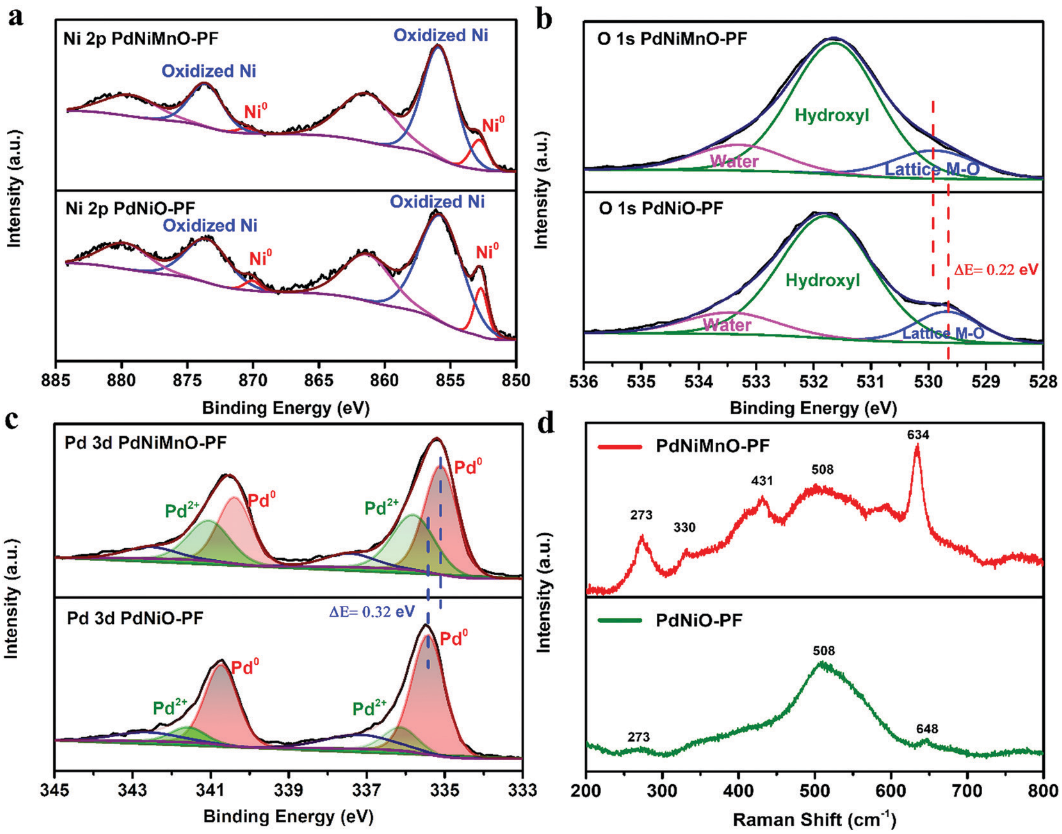

Fig. 2 Spectroscopic characterizations of PdNiMnO-PF. High-resolution XPS spectra of (a) Ni 2p, (b) O 1s and (c) Pd 3d for PdNiMnO-PF (top) and PdNiO-PF (bottom). (d) Raman spectra of PdNiMnO-PF (top) and PdNiO-PF (bottom).

PdNiO-PF. Other weaker lines located at 273 cm^{-1} and 330 cm^{-1} were assigned to the resonance/secondary scattering effect.[45] The spectroscopic analyses are consistent with TEM results, confirming the strengthened SMSI effect for surface catalysis.

To further understand the Pd, Ni, and Mn interactions in the PdNiMn-PF, X-ray absorption spectroscopy (XAS) was carried out to probe the electronic state and atomic local structure.[48,51,52] X-Ray absorption near edge structure (XANES) of the PdNiMn film indicated that all three metals (Pd, Ni, and Mn) remained in the metallic form (Fig. S8, ESI†). However, there are some differences between metallic states in the reference samples and alloy states, indicating some interactions between Pd, Ni, and Mn, which could be due to the formation of Pd–Ni/Mn bonds, resulting in electron transfer between Pd, Ni, and Mn to promote the reaction kinetics. The extended X-ray absorption fine structure (EXAFS) further confirmed those interactions (Fig. 3). On comparing metallic Pd with Pd in PdNi and PdNiMn in Fourier-transform EXAFS (Fig. 3a), the locations of the first peak (2.2 Å) of PdNi and PdNiMn was lower than that of the metallic bonding Pd–Pd peak (2.5Å), which means that Pd formed a new shorter bond with Ni. The 2D wavelet transform of the Pd K-edge also confirmed that Pd formed new bonds with Ni due to the new peak formation at around 7 Å^{-1} (Fig. 3b and Fig. S9, ESI†) that was not present in the metallic Pd. After the addition of Mn, the first peak at around 2.2 Å in the Mn K-edge was also smaller than the metallic Mn–Mn peak at around 2.4 Å (Fig. 3a), which can be attributed to the shorter Mn–Ni bonds. It is hard to see the difference in the Ni K-edge and Pd K-edge due to the addition of a small amount of Mn. However, when carefully checking the wavelet transform of the Mn K-edge between PdNiMn and metallic Mn, the second peak at around 8.6 Å^{-1} in PdNiMn is broader than the one seen for metallic Mn (Fig. 3b and Fig. S9, ESI†). The peak intensity and shape of both the Ni K-edge and Pd K-edge in PdNiMn and PdNi changed, suggesting that Mn interacts with both Ni and Pd to form new bonds. Therefore, the XAS results verified that Mn was bonded with both Pd and Ni in PdNiMn, which is consistent with TEM analyses and could be the reason for the promotion of the surface oxygenation in the catalysts.

The well-constructed 3D porous structure of PdNiMnO-PF synthesized by anodization benefits the Pd-support interaction for surface catalysis and ensures the intimate contact between catalysts and electrolytes (Fig. 4a). The electron-rich character of Pd is responsible for the promotion of O–O cleavage and facilitates ORR reaction kinetics.[17,53] The electrocatalytic ORR performance of the catalysts was evaluated using a three-electrode cell in 0.1 M KOH with a rotating ring disk electrode (RRDE) as the working electrode to study the intrinsic electron transfer number (n) and hydrogen peroxide yield ($\chi_{H_2O_2}$(%)) for the ORR. All voltages mentioned below were referred to the

Published on 18 February 2022. Downloaded by University of Central Florida on 4/7/2022 4:15:53 PM.

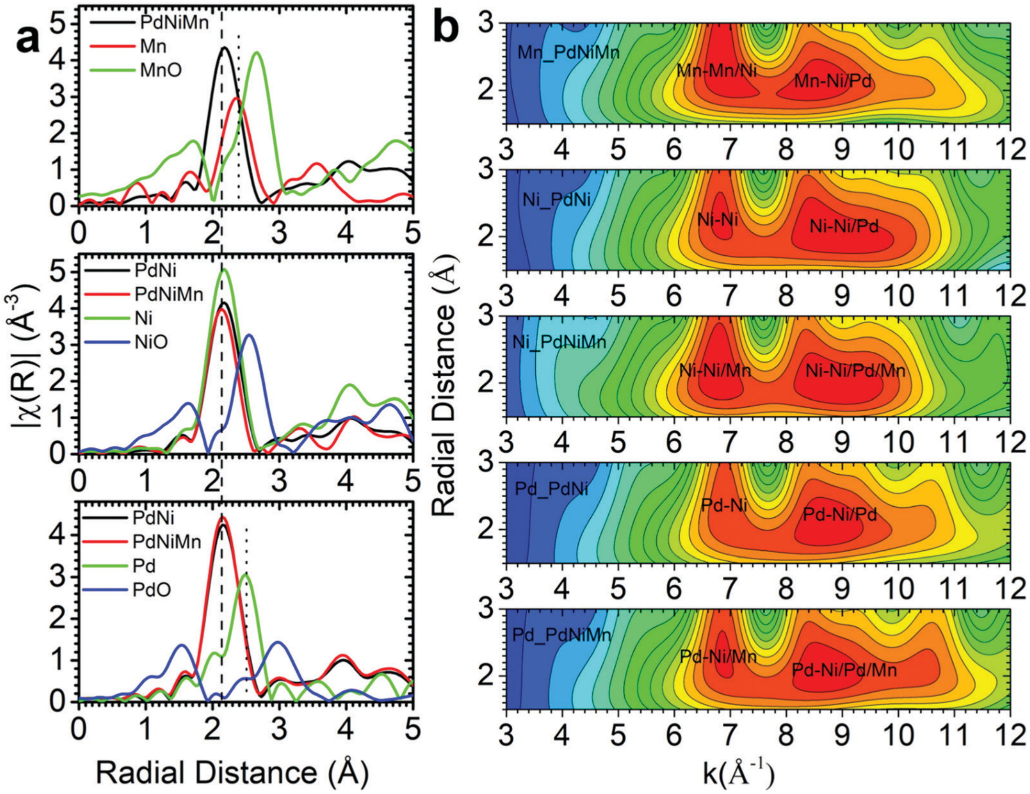

Fig. 3 XAS characterizations. (a) Fourier Transform *R*-space of Mn K-edge, Ni K-edge, and Pd K-edge (from top to bottom), the dash indicates Mn–Ni/Mn, Ni–Mn/Ni/Pd, and Pd–Mn/Ni/Pd bonds, the dotted line indicates Mn–Mn and Pd–Pd bonds. (b) Wavelet transform of the Mn K-edge for PdNiMn, Ni K-edge for PdNi, Ni K-edge for PdNiMn, Pd K-edge for PdNi, and Pd K-edge for PdNiMn (from top to bottom).

reversible hydrogen electrode (RHE). Cathodic peaks located at 0.82 and 0.70 V were observed in the cyclic voltammetry (CV) curves recorded in O_2-saturated electrolyte for PdNiMnO-PF, corresponding to O_2 and Pd–O reduction peaks, respectively (Fig. 4b).[54] Only the Pd–O reduction peak (0.70 V) was observed in the N_2-saturated electrolyte, confirming an apparent Pd–O reduction and surface oxygenation on the catalyst. Note that the current density of the Pd–O reduction peak in CV curves for PdNiMnO-PF is significantly higher than that for PdNiO-PF and PdNiMn metal porous film (PdNiMn-MPF, Fig. S10, ESI†). This further confirms the presence of the oxygenated Pd in PdNiMnO-PF with a higher degree of surface oxygenation. Note that we compared PdNiMnO-PF with PdNiMn-MPF to verify the efficacy of the SMSI effect.

Linear sweep voltammetry (LSV) was conducted at 1600 rpm to further explore the ORR performance and electron transfer pathways of the catalysts. The n and $\chi_{H_2O_2}(\%)$ of PdNiMnO-PF and other control catalysts measured at 0.4 V are summarized in Fig. 4c. PdNiMnO-PF (Fig. S11a, ESI†) showed a negligible H_2O_2 yield (5.6%) and enhanced electron transfer kinetics (n = 3.89, Fig. S11b, ESI†), which are much better than the control samples (PdNiMn film, PdNiMn-MPF, and PdNiO-PF) and comparable to the Pd/C catalyst. This implies that the surface oxygenation and porous structure improved the electron transfer towards the complete 4-electron pathway and significantly suppressed the H_2O_2 production.[24,35] The LSV curves (Fig. S12, ESI†) were further analyzed to evaluate the ORR activities of the catalysts by checking the onset potential when the current density exceeded 0.1 mA cm^{-2} (E_{onset}), half-wave potential ($E_{1/2}$), and diffusion-limiting current (J_d), which are summarized in Fig. 4d. The PdNiMnO-PF shows a more positive E_{onset} of 0.94 V and $E_{1/2}$ of 0.84 V than PdNiO-PF and PdNiMn-MPF, and comparable to Pd/C. Also, the PdNiMnO-PF exhibited a higher J_d of 6.3 mA cm^{-2} as compared to PdNiMn-MPF (5.2 mA cm^{-2}), PdNiO-PF (6.2 mA cm^{-2}), and Pd/C (5.7 mA cm^{-2}), which is very close to the theoretical value of J_d of 6 mA cm^{-2} at a rotating speed of 1600 rpm and the higher value is ascribed to the porous structure.[55] The overall ORR performance of PdNiMnO-PF is superior to the control catalysts, convincing of the merits of the enhanced Pd-support interaction. To further verify the significance of surface oxygenation in promoting the ORR performance, we prepared PdNiMnO-PF with different oxygenation degrees by tuning the H_2O content added to the anodization electrolytes. The catalysts showed slightly different ORR performance (Fig. S13, ESI†) by varying the oxygenation degrees with the PdNiMnO-PF (2M) sample showing the optimal ORR performance (Table S3, ESI†) and highest Pd–O reduction area, which confirmed the relation between the surface oxygenation and ORR performance. In addition, the PdNiMnO-PF showed a much higher specific activity (SA) of 253 μA cm$^{-2}_{\text{Pd}}$ than those of Pd/C (233 μA cm$^{-2}_{\text{Pd}}$), PdNiO-PF (160 μA cm$^{-2}_{\text{Pd}}$), and

This journal is © The Royal Society of Chemistry 2022

Published on 18 February 2022. Downloaded by University of Central Florida on 4/7/2022 4:15:53 PM.

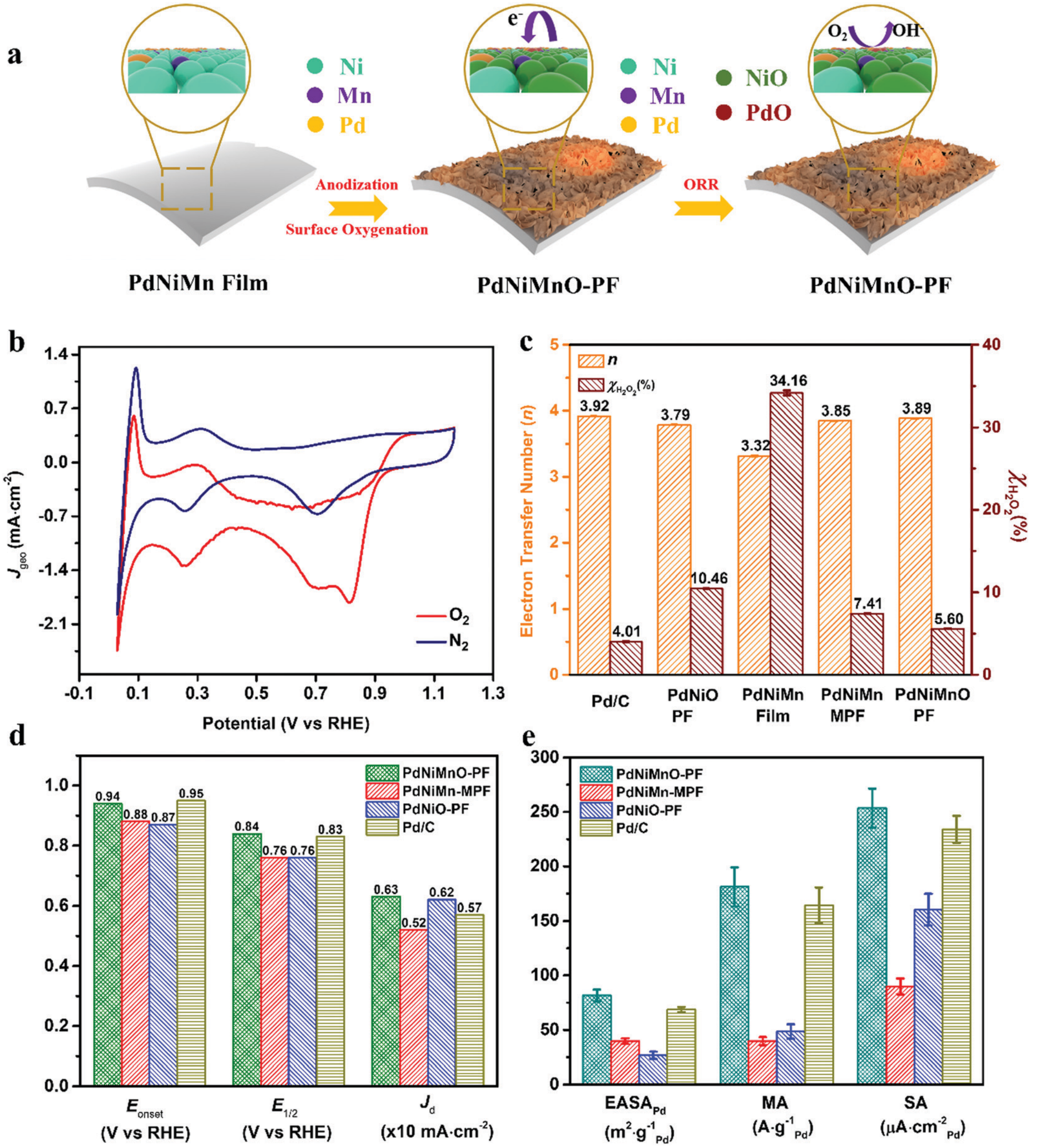

Fig. 4 Electrochemical Performance. (a) Schematic illustration of surface oxygenation and the working principle of the PdNiMnO-PF catalyst during the ORR. (b) Cyclic voltammetry (CV) curves of PdNiMnO-PF performed in O_2- and N_2-saturated electrolytes. (c) Comparison of electron transfer number (*n*) and hydrogen peroxide yield ($\chi_{H_2O_2}$(%)) for Pd/C, PdNiO-PF, PdNiMn film, PdNiMn-MPF and PdNiMnO-PF under 0.4 V (V *VS.* RHE). (d) Comparison of E_{onset}, $E_{1/2}$, and J_d for PdNiMnO-PF, PdNiMn-MPF, PdNiO-PF, and Pd/C. (e) Comparison of $EASA_{Pd}$, MA, and SA for PdNiMnO-PF, PdNiMn-MPF, PdNiO-PF, and Pd/C.

PdNiMn-MPF (90 μA $cm^{-2}{}_{Pd}$, Fig. 4e), indicating the greatly improved utilization efficiency of Pd embedded in the porous structure. The PdNiMnO-PF also delivered a remarkedly larger mass activity (MA) of 180.9 A $g^{-1}{}_{pd}$ than those of Pd/C (163.6 A $g^{-1}{}_{pd}$), PdNiO-PF (48.4 A $g^{-1}{}_{pd}$), and PdNiMn-MPF (39.7 A $g^{-1}{}_{pd}$). Furthermore, the PdNiMnO-PF showed a higher $EASA_{Pd}$ of 81.9 m^2 $g^{-1}{}_{Pd}$ than those of Pd/C (68.7 m^2 $g^{-1}{}_{Pd}$), PdNiO-PF (26.6 m^2 $g^{-1}{}_{Pd}$), and PdNiMn-MPF (39.75 m^2 $g^{-1}{}_{Pd}$), indicating the significantly increased accessible surface area of the catalysts to the electrolyte.[56] Chronoamperometry testing (Fig. S14, ESI†) was performed to investigate the electrochemical stability of PdNiMnO-PF at 0.6 V in O_2-saturated 0.1 M KOH electrolyte, which showed improved stability and higher current retention (83.6%) than Pd/C (71.3%) after 12 hours of stability testing, due to the inhibited Pd deactivation in the oxygenated support.[20,30]

We performed the first-principles density functional theory (DFT) calculations to gain insight into the role of Mn in affecting the activity and durability of the PdNiMnO-PF catalyst. Our calculations predicted that Mn was energetically more favorable to be doped in the sublayer than the outermost layer of the Pd(111) surface (as shown in Fig. S15, ESI† and denoted as Mn-Pd(111)). Fig. S16 (ESI†) shows that the free energy changes for all the elementary steps of the ORR on

Published on 18 February 2022. Downloaded by University of Central Florida on 4/7/2022 4:15:53 PM.

Mn-Pd(111) became negative under an electrode potential of 0.71 V, higher than that of 0.68 V for the ORR on undoped Pd(111). This result indicates that sublayer Mn weakens the interaction between Pd and ORR intermediates and thus enhances the ORR activity of Pd(111). Moreover, the enthalpy change for the demetallation of a Pd atom from the outermost layer of Mn-Pd(111) was predicted to be 4.71 eV, higher than that of 4.66 eV for that from undoped Pd(111), suggesting that the sublayer Mn could also stabilize the outermost surface Pd atoms (Fig. S17, ESI†). In conclusion, our DFT results reveal that subsurface Mn could enhance the ORR activity and stability of Pd catalysts, explaining well our experimental observations in Fig. 4.

We conducted TEM, SEM, XRD, XPS, UPS, and Raman studies to verify the structural integrity of PdNiMnO-PF after the stability test. The structure and composition of the catalyst after the stability test (denoted as PdNiMnO-stability) are consistent with the fresh catalyst, as proved by HRTEM and STEM-HAADF images (Fig. S18, ESI†), as well as EDS mappings (Fig. S19, ESI†). As confirmed by SEM images (Fig. S20, ESI†), the porous structure of PdNiMnO-PF was well maintained without collapse after the stability test. XRD (Fig. S5, ESI†) results show the intact structure of PdNiMnO-stability as compared with the fresh catalyst. Moreover, XPS (Fig. S21, ESI†) and UPS (Fig. S22, ESI†) were employed to investigate the electronic structure of PdNiMnO-stability. The XPS Ni 2p spectrum shows the presence of Ni^{2+} (855.8 and 873.6 eV) and largely decreased Ni^0 (852.8 and 870.2 eV).[57] The XPS Pd 3d spectrum shows Pd^0 (335.18 and 340.45 eV) and Pd^{2+} (335.96 and 341.23 eV), implying a negligible BE change as compared to the fresh catalyst. Also, the XPS O 1s spectrum displays the BE of lattice oxygen at 529.86 eV, similar to the fresh catalyst.[44] Moreover, the WF of PdNiMnO-stability estimated by UPS is 4.76 eV, consistent with the fresh catalyst. Besides, Raman shifts (Fig. S23, ESI†) of PdNiMnO, located at 273 cm^{-1}, 330 cm^{-1}, 431 cm^{-1}, and 634 cm^{-1}, are attributed to Pd–O. It is noteworthy that a new stretching vibration mode appears at around 555 cm^{-1}, except for the Ni–O at 508 cm^{-1} as compared to the fresh catalyst due to the formation of $Ni(OH)_2$,[58] which was also confirmed by the lattice fringe of 0.233 nm identified from HRTEM (Fig. S18, ESI†), corresponding to the plane of $Ni(OH)_2$ (101). This surface reconstruction on the oxygenated Ni could largely impede the detachment of Pd into the electrolyte due to circumvented Ni leaching and the associated chemical/physical blockage of dissolution of Pd.[59,60] Moreover, the TEM-EDS and XPS elemental composition analysis demonstrated high consistency before and after the stability test (Table S4, ESI†). Therefore, the strong metal-support interaction and surface reconstruction could synergistically stabilize Pd during the alternative ORR/OER process in an alkaline environment. The microscopic and spectroscopic characterizations confirmed the structural and electronic structure integrity of PdNiMnO-PF after the electrochemical stability test.

We further examined the OER activity of PdNiMnO-PF by checking LSV curves (Fig. S24, ESI†). A potential (@10 mA cm^{-2}) of 1.59 V was obtained for PdNiMnO-PF, the same for PdNiO-PF (1.59 V) and superior to NiMnO-PF (1.65 V). Also, the significantly inferior OER performance of Pd/C as compared to PdNiMnO-PF suggests that Pd has no activity towards the OER, indicating that NiMnO is the active phase for the OER.[36] The superior OER performance of PdNiMnO-PF as compared to other control catalysts confirms the efficacy of the Pd/FOS catalyst due to strong SMSI. Therefore, a rationally designed electrode can be achieved by utilizing Pd as the ORR active site embedded in the NiMnO functional support (OER active phase) through SMSI in the porous network that can synergistically behave as a highly efficient bifunctional catalyst for ZAB.

Based on the superiority of the overall potential difference between the ORR($E_{1/2}$) and OER($E_{@10\ \mathrm{mA\ cm}^{-2}}$) for PdNiMnO-PF as compared to other catalysts (Fig. S25, ESI†), rechargeable zinc–air flow batteries (ZAFB) were assembled using PdNiMnO-PF as the cathode catalysts and Zn plates as the anodes (Fig. 5a). The OCP of ZAFB (PdNiMnO) was measured to be 1.37 V (V *vs.* Zn/Zn^{2+} for zinc–air battery), higher than that of ZAFB (Pt/C-RuO_2) (1.35 V, Fig. S26, ESI†). A green LED lamp was lit up by two ZAFBs (PdNiMnO) connected in series (Fig. S27, ESI†). A peak power density of 211.6 mW cm^{-2} at a current density of 377 mA cm^{-2} (Fig. 5b) was achieved for ZAFB (PdNiMnO), surpassing that of ZAFB (Pt/C-RuO_2) (106.2 mW cm^{-2} at 234 mA cm^{-2}). Moreover, the ZAFB (PdNiMnO) delivered a specific capacity and energy density of 812.9 mA h g^{-1} and 958 W h kg^{-1}, respectively, superior to those of ZAFB (Pt/C-RuO_2) (779.1 mA h g^{-1} and 860.3 W h kg^{-1}, Fig. S28, ESI†). Discharge curves at various current densities (5–50 mA cm^{-2}) are shown in Fig. 5c to evaluate the rate capacity of ZAFB. The ZAFB (PdNiMnO) shows more prominent discharge capacities at higher current densities (10–50 mA cm^{-2}) than ZAFB (Pt/C-RuO_2), proving the facilitated reaction kinetics enabled by the enhanced Pd-support interaction of PdNiMnO-PF. The voltage gap (ΔV) between the charge/discharge potential difference during ZAFB operation and peak power density of ZAFB (PdNiMnO) is illustrated in the characteristic plot (Fig. 5d) to compare with other state-of-the-art catalysts. The ZAFB (PdNiMnO) delivered an optimized performance regarding the voltage gap and power density (Table S5, ESI†) among the state-of-the-art catalysts for ZAB, including PGM-based materials,[11,48,57,61] transition metal-based materials,[62–64] carbon-based composites,[65–71] and some emerging single-atom catalysts.[72] The superior performance as compared to the state-of-the-art catalysts results from the seamless Pd/FOS interaction that contributes to the fast mass/electron transport, ensuring the stabilization of Pd in the FOS network.

To confirm that the oxidation of Pd experienced during the charging process will not impact the activity and stability of the ZAFB, we performed XPS characterization on probing the chemical state and composition of Pd right after the charging process of the last cycle (65 hours, 130 cycles) at a current density of 10 mA cm^{-2}. As expected, Pd formed a more oxidized state (71.4%) after the charging process, revealed by high-resolution XPS Pd 3d spectra (Fig. S29a, ESI†), in contrast

Published on 18 February 2022. Downloaded by University of Central Florida on 4/7/2022 4:15:53 PM.

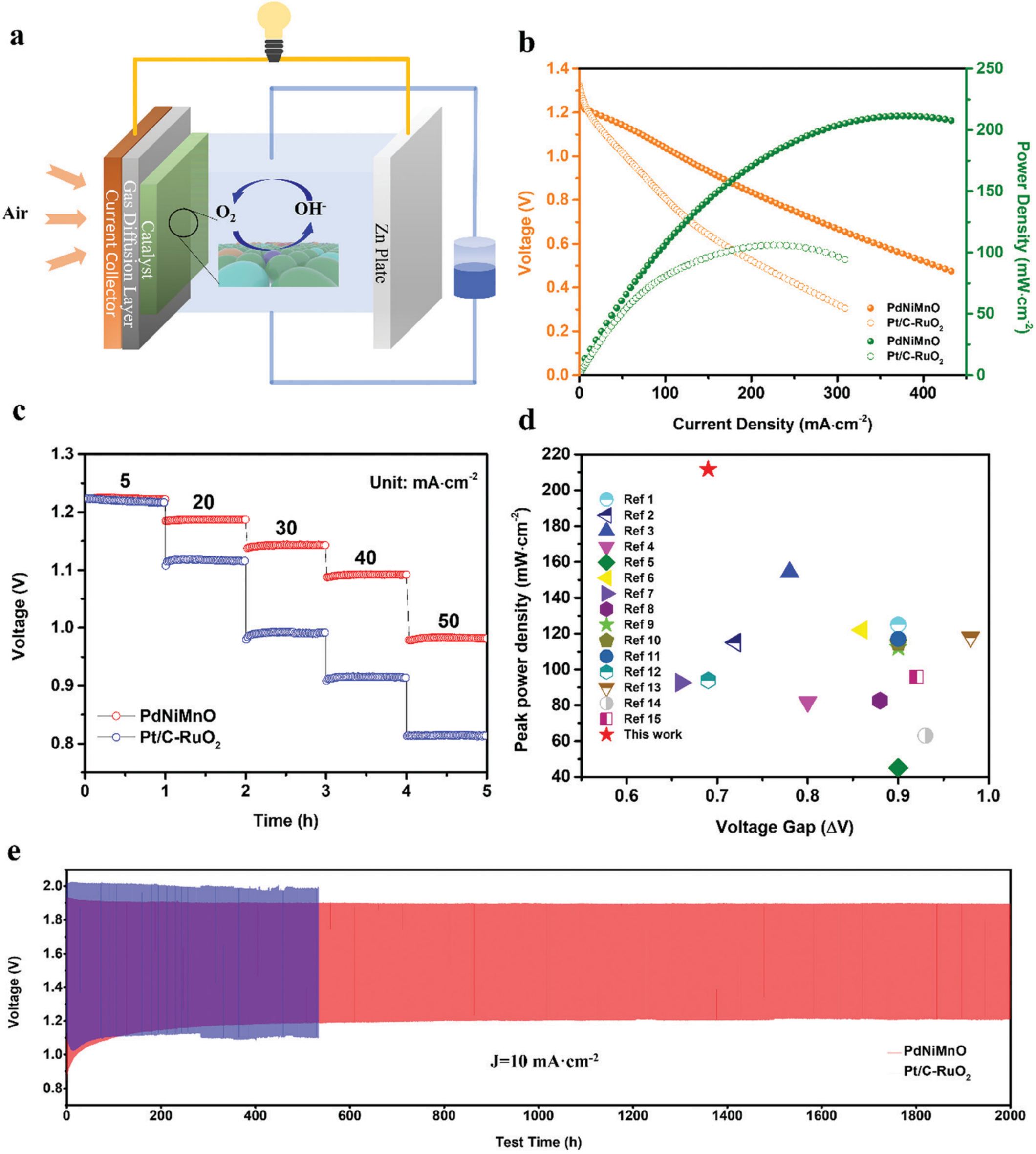

Fig. 5 ZAFB performance. (a) Schematic illustration of the working principle of an aqueous zinc–air flow battery. (b) Comparison of polarization and power density curves for PdNiMnO and Pt/C-RuO_2. (c) Comparison of the discharging behavior of PdNiMnO and Pt/C-RuO_2-based ZAFBs at various current densities. (d) A characteristic plot of peak power density *vs.* voltage gap for this work and other references. (e) Long-term Galvanostatic discharge–charge cycling stability of ZAFB (PdNiMnO) at a current density of 10 mA cm^{-2}.

to a more metallic state (66.7%) before charging (Fig. S29b, ESI†). However, this oxidation of Pd after charging will not affect the excellent performance of ZAFB in a long-term operation due to the metallic Pd being reversibly formed during the discharging process, as confirmed by the reduced voltage gap read from Fig. S29c (ESI†). The stability of ZAFB (PdNiMnO) was tested by performing charging/discharging cycling at 10 mA cm^{-2} (Fig. 5e) for 2000 h (4000 cycles), which did not show any performance degradation. On the other hand, the voltage gap of 1 V (first 10 h cycles) gradually decreased to 0.69 V (last 10 h cycles, Fig. S30, ESI†), outperforming the ZAFB (Pt/C-RuO_2). This remarkable cycling stability of ZAFB (PdNiMnO) proves the merits of the SMSI effect in inhibiting Pd deactivation through strengthening the Pd-support interaction using oxygenated functional support,[17,20,34] thus confirming the novelty of the seamless interaction between countless Pd/FOS interfaces enabled by the surface oxygenation strategy as compared with other state-of-the-art catalysts. The proposed concept of the coupling of low-PGMs with functional oxygenated support provides a new strategy for bifunctional catalyst design possessing countless and seamless interfaces.

Conclusion

We have rationally designed and verified the SMSI effect by promoting surface oxygenation in the porous film *via*

Published on 18 February 2022. Downloaded by University of Central Florida on 4/7/2022 4:15:53 PM.

Mn-doping. The strengthened Pd-support interaction tailors the electronic structure of Pd active sites for the ORR due to the strong coupling with neighboring oxygenated catalysts, redistributing the local electron density. As a result, the accelerated electron transfer and boosted reaction kinetics were achieved in the PdNiMnO-PF for the ORR in addition to the secondary adsorption sites for the intermediates. The oxygenated support also served as the active phase for the OER, enabling the PdNiMnO-PF bifunctional abilities for ZAFB. As a proof of concept, the ZAFB (PdNiMnO) delivered significantly improved cyclability (over 2000 h, 4000 cycles) and peak power density of 211.6 mW cm^{-2}, as well as a greatly reduced voltage gap (0.69 V). The proposed concept of low-Pd/functionally oxygenated support interaction sheds light on the design of novel catalysts for various electrochemical energy applications.

Author contributions

Y. Y. conceived the concept and led the project. W. Z. synthesized the materials and conducted the electrochemical measurements. W. Z., G. W., and Z. L. performed SEM, XPS, UPS, XRD, and Raman characterizations. Y. Z. and M. G. conducted the TEM characterization. W. Z. analyzed the TEM data under the direction of Y. Z. M. W., H. Z., and Z. F. performed the XAS measurements and analyses and wrote the corresponding XAS section. B. L. and G. W. performed DFT calculations. W. Z. analyzed the data and wrote the manuscript. J. C. and Y. Y. oversaw all the results and revised the manuscript. All authors approved the manuscript.

Nomenclature

SMSI	Strong metal support interaction FOS functionally oxygenated supports
PGMs	Platinum group metals EDS energy-dispersive X-ray spectroscopy
ORR	Oxygen reduction reaction OER oxygen evolution reaction
PF	Porous film BE binding energy
ZAFB	Zinc–air flow batteries ZAB zinc–air batteries
XRD	X-ray diffraction UPS ultraviolet photoelectron spectroscopy
XPS	X-ray photoelectron spectroscopy WF work function
SEM	Scanning electron microscopy TEM transmission electron microscopy
ECSA	Electrochemically active surface area XAS X-ray absorption spectroscopy
OCP	Open circuit potential CV cyclic voltammetry
RHE	Reversible hydrogen electrode LSV linear sweep voltammetry
n	Electron transfer number
$\chi_{H_2O_2}$(%)	Hydrogen peroxide yield
E_{onset}	Onset potential
$E_{1/2}$	Half-wave potential
J_{d}	Diffusion-limiting current
SA	Specific activity
MA	Mass activity
EDLC	Electrical double layer capacitance
RRDE	Rotating ring disk electrode
EXAFS	Extended X-ray absorption fine structure
XANES	X-ray absorption near edge structure
EIS	Electrochemical impedance spectroscopy
HAADF-STEM	High-angle annular dark-field scanning transmission electron microscopy

Conflicts of interest

The authors declare no conflict of interest.

Acknowledgements

Y. Y. thanks the support by the National Science Foundation under Grant No. CMMI-1851674, CBET-194984, and the startup grant from the University of Central Florida. The XPS characterization was supported by the National Science Foundation NSF MRI: XPS: ECCS: 1726636, hosted in MCF-AMPAC facility, MSE, CECS, UCF. The Raman characterization was supported by the National Science Foundation under Grant No. DMR 1920050 (MRI). The XAS characterization (Z. F.) was supported by the National Science Foundation under Grant No. CBET-1949870 and CBET-2016192. The use of the Advanced Photon Source at Argonne National Laboratory for XAS measurements at beamlines 12BM was supported by the US Department of Energy under contract no. DE-AC02-06CH11357. Y. Z. and M. G. acknowledge the supports of the National Science Foundation of China (No. 12004156), and Shenzhen Basic Research Fund (JCYJ20190809181601639). The TEM work (Y. Z. and M. G.) used the resources of the Pico Center from SUSTech Core Research Facilities that receive support from the Presidential Fund and Development and Reform Commission of Shenzhen Municipality. G. W. and B. L. acknowledge support from the US National Science Foundation (DMR 1905572). Computational resources were provided by the University of Pittsburgh Center for Research Computing as well as the Extreme Science and Engineering Discovery Environment, which is supported by National Science Foundation under grant no. ACI-1053575.

References

1 L. Trahey, F. R. Brushett, N. P. Balsara, G. Ceder, L. Cheng, Y.-M. Chiang, N. T. Hahn, B. J. Ingram, S. D. Minteer, J. S. Moore, K. T. Mueller, L. F. Nazar, K. A. Persson, D. J. Siegel, K. Xu, K. R. Zavadil, V. Srinivasan and G. W. Crabtree, *Proc. Natl. Acad. Sci. U. S. A.*, 2020, **117**, 12550.

2 Z. P. Cano, D. Banham, S. Ye, A. Hintennach, J. Lu, M. Fowler and Z. Chen, *Nat. Energy*, 2018, **3**, 279–289.

3 J. Fu, Z. P. Cano, M. G. Park, A. Yu, M. Fowler and Z. Chen, *Adv. Mater.*, 2017, **29**, 1604685.

This journal is © The Royal Society of Chemistry 2022

Published on 18 February 2022. Downloaded by University of Central Florida on 4/7/2022 4:15:53 PM.

4 J. Chang, G. Wang and Y. Yang, *Small Sci.*, 2021, **1**, 2100044.

5 J. Zhang, Z. Zhao, Z. Xia and L. Dai, *Nat. Nanotechnol.*, 2015, **10**, 444–452.

6 Y. Nie, L. Li and Z. Wei, *Chem. Soc. Rev.*, 2015, **44**, 2168–2201.

7 S. Ren, X. Duan, S. Liang, M. Zhang and H. Zheng, *J. Mater. Chem. A*, 2020, **8**, 6144–6182.

8 X. Wang, Z. Li, Y. Qu, T. Yuan, W. Wang, Y. Wu and Y. Li, *Chem*, 2019, **5**, 1486–1511.

9 M. Li, Z. Zhao, T. Cheng, A. Fortunelli, C.-Y. Chen, R. Yu, Q. Zhang, L. Gu, B. V. Merinov, Z. Lin, E. Zhu, T. Yu, Q. Jia, J. Guo, L. Zhang, W. A. Goddard, Y. Huang and X. Duan, *Science*, 2016, 1414.

10 C. Chen, Y. Kang, Z. Huo, Z. Zhu, W. Huang, H. L. Xin, J. D. Snyder, D. Li, J. A. Herron, M. Mavrikakis, M. Chi, K. L. More, Y. Li, N. M. Markovic, G. A. Somorjai, P. Yang and V. R. Stamenkovic, *Science*, 2014, 1339.

11 M. Luo, Z. Zhao, Y. Zhang, Y. Sun, Y. Xing, F. Lv, Y. Yang, X. Zhang, S. Hwang, Y. Qin, J.-Y. Ma, F. Lin, D. Su, G. Lu and S. Guo, *Nature*, 2019, **574**, 81–85.

12 G. Wang, J. Chang, S. Koul, A. Kushima and Y. Yang, *J. Am. Chem. Soc.*, 2021, **143**, 11595–11601.

13 W. Xia, A. Mahmood, Z. Liang, R. Zou and S. Guo, *Angew. Chem., Int. Ed.*, 2016, **55**, 2650–2676.

14 Y. Yang, M. Luo, W. Zhang, Y. Sun, X. Chen and S. Guo, *Chem*, 2018, **4**, 2054–2083.

15 M. Shao, Q. Chang, J.-P. Dodelet and R. Chenitz, *Chem. Rev.*, 2016, **116**, 3594–3657.

16 Y. Zhong, X. Xu, W. Wang and Z. Shao, *Batteries Supercaps*, 2019, **2**, 272–289.

17 Q. Jia, S. Ghoshal, J. Li, W. Liang, G. Meng, H. Che, S. Zhang, Z.-F. Ma and S. Mukerjee, *J. Am. Chem. Soc.*, 2017, **139**, 7893–7903.

18 S. J. Tauster, S. C. Fung, R. T. K. Baker and J. A. Horsley, *Science*, 1981, 1121.

19 L. Zhang, L. Wang, C. M. B. Holt, T. Navessin, K. Malek, M. H. Eikerling and D. Mitlin, *J. Phys. Chem. C*, 2010, **114**, 16463–16474.

20 Y. Lu, Y. Jiang, X. Gao, X. Wang and W. Chen, *J. Am. Chem. Soc.*, 2014, **136**, 11687–11697.

21 E. Antolini, J. R. C. Salgado and E. R. Gonzalez, *J. Power Sources*, 2006, **160**, 957–968.

22 W. Gao, Z. Zhang, M. Dou and F. Wang, *ACS Catal.*, 2019, **9**, 3278–3288.

23 Y. Liu and W. E. Mustain, *J. Am. Chem. Soc.*, 2013, **135**, 530–533.

24 Z.-F. Huang, J. Song, S. Dou, X. Li, J. Wang and X. Wang, *Matter*, 2019, **1**, 1494–1518.

25 S. J. Tauster, S. C. Fung and R. L. Garten, *J. Am. Chem. Soc.*, 1978, **100**, 170–175.

26 S. Shan, J. Li, Y. Maswadeh, C. O'Brien, H. Kareem, D. T. Tran, I. C. Lee, Z.-P. Wu, S. Wang, S. Yan, H. Cronk, D. Mott, L. Yang, J. Luo, V. Petkov and C.-J. Zhong, *Nat. Commun.*, 2020, **11**, 4201.

27 C. Jackson, G. T. Smith, D. W. Inwood, A. S. Leach, P. S. Whalley, M. Callisti, T. Polcar, A. E. Russell, P. Levecque and D. Kramer, *Nat. Commun.*, 2017, **8**, 15802.

28 H. Xu, H. Shang, C. Wang and Y. Du, *Small*, 2021, **17**, 2005092.

29 Y. Feng, Q. Shao, Y. Ji, X. Cui, Y. Li, X. Zhu and X. Huang, *Sci. Adv.*, 2018, **4**, eaap8817.

30 A. Chen and C. Ostrom, *Chem. Rev.*, 2015, **115**, 11999–12044.

31 W. Xiao, M. A. Liutheviciene Cordeiro, M. Gong, L. Han, J. Wang, C. Bian, J. Zhu, H. L. Xin and D. Wang, *J. Mater. Chem. A*, 2017, **5**, 9867–9872.

32 K. Liang, L. Guo, K. Marcus, S. Zhang, Z. Yang, D. E. Perea, L. Zhou, Y. Du and Y. Yang, *ACS Catal.*, 2017, **7**, 8406–8412.

33 K. A. Stoerzinger, M. Risch, B. Han and Y. Shao-Horn, *ACS Catal.*, 2015, **5**, 6021–6031.

34 H.-S. Oh, H. N. Nong, T. Reier, A. Bergmann, M. Gliech, J. Ferreira de Araújo, E. Willinger, R. Schlögl, D. Teschner and P. Strasser, *J. Am. Chem. Soc.*, 2016, **138**, 12552–12563.

35 X. Shen, T. Nagai, F. Yang, L. Q. Zhou, Y. Pan, L. Yao, D. Wu, Y.-S. Liu, J. Feng, J. Guo, H. Jia and Z. Peng, *J. Am. Chem. Soc.*, 2019, **141**, 9463–9467.

36 Q. Wang, X. Huang, Z. L. Zhao, M. Wang, B. Xiang, J. Li, Z. Feng, H. Xu and M. Gu, *J. Am. Chem. Soc.*, 2020, **142**, 7425–7433.

37 J. Yin, Y. Li, F. Lv, Q. Fan, Y.-Q. Zhao, Q. Zhang, W. Wang, F. Cheng, P. Xi and S. Guo, *ACS Nano*, 2017, **11**, 2275–2283.

38 C. C. L. McCrory, S. Jung, J. C. Peters and T. F. Jaramillo, *J. Am. Chem. Soc.*, 2013, **135**, 16977–16987.

39 A. Allagui, T. J. Freeborn, A. S. Elwakil and B. J. Maundy, *Sci. Rep.*, 2016, **6**, 38568.

40 J. Lin, H. Jia, H. Liang, S. Chen, Y. Cai, J. Qi, C. Qu, J. Cao, W. Fei and J. Feng, *Adv. Sci.*, 2018, **5**, 1700687.

41 T.-J. Wang, F.-M. Li, H. Huang, S.-W. Yin, P. Chen, P.-J. Jin and Y. Chen, *Adv. Funct. Mater.*, 2020, **30**, 2000534.

42 H. Huang, J. Liu, P. Sun, S. Ye and B. Liu, *RSC Adv.*, 2017, **7**, 7406–7412.

43 D. Wang, Q. Li, C. Han, Q. Lu, Z. Xing and X. Yang, *Nat. Commun.*, 2019, **10**, 3899.

44 M. A. Peck and M. A. Langell, *Chem. Mater.*, 2012, **24**, 4483–4490.

45 O. Lupan, V. Postica, M. Hoppe, N. Wolff, O. Polonskyi, T. Pauporté, B. Viana, O. Majérus, L. Kienle, F. Faupel and R. Adelung, *Nanoscale*, 2018, **10**, 14107–14127.

46 S. Jayabal, G. Saranya, D. Geng, L.-Y. Lin and X. Meng, *J. Mater. Chem. A*, 2020, **8**, 9420–9446.

47 M. S. Ureta-Zañartu, C. Berríos, J. Pavez, J. Zagal, C. Gutiérrez and J. F. Marco, *J. Electroanal. Chem.*, 2003, **553**, 147–156.

48 F. Pan, Z. Li, Z. Yang, Q. Ma, M. Wang, H. Wang, M. Olszta, G. Wang, Z. Feng, Y. Du and Y. Yang, *Adv. Energy Mater.*, 2021, **11**, 2002204.

49 M. Sharma, J.-H. Jang, D. Y. Shin, J. A. Kwon, D.-H. Lim, D. Choi, H. Sung, J. Jang, S.-Y. Lee, K. Y. Lee, H.-Y. Park, N. Jung and S. J. Yoo, *Energy Environ. Sci.*, 2019, **12**, 2200–2211.

50 W. Liu, C. Lu, X. Wang, K. Liang and B. K. Tay, *J. Mater. Chem. A*, 2015, **3**, 624–633.

51 M. Wang, L. Árnadóttir, Z. J. Xu and Z. Feng, *Nano-Micro Lett.*, 2019, **11**, 47.

Published on 18 February 2022. Downloaded by University of Central Florida on 4/7/2022 4:15:53 PM.

52 H. Liao, C. Wei, J. Wang, A. Fisher, T. Sritharan, Z. Feng and Z. J. Xu, *Adv. Energy Mater.*, 2017, **7**, 1701129.

53 R. Zhang, L. Wang, Y.-H. Ma, L. Pan, R. Gao, K. Li, X. Zhang and J.-J. Zou, *J. Mater. Chem. A*, 2019, **7**, 10010–10018.

54 C. Qiu, S. Wang, R. Gao, J. Qin, W. Li, X. Wang, Z. Zhai, D. Tian and Y. Song, *Mater. Today Energy*, 2020, **18**, 100557.

55 D. C. Nguyen, D. T. Tran, T. L. L. Doan, D. H. Kim, N. H. Kim and J. H. Lee, *Adv. Energy Mater.*, 2020, **10**, 1903289.

56 G. Wang, Z. Yang, Y. Du and Y. Yang, *Angew. Chem., Int. Ed.*, 2019, **58**, 15848–15854.

57 Z. Li, W. Niu, Z. Yang, N. Zaman, W. Samarakoon, M. Wang, A. Kara, M. Lucero, M. V. Vyas, H. Cao, H. Zhou, G. E. Sterbinsky, Z. Feng, Y. Du and Y. Yang, *Energy Environ. Sci.*, 2020, **13**, 884–895.

58 B. S. Yeo and A. T. Bell, *J. Phys. Chem. C*, 2012, **116**, 8394–8400.

59 Y. Zhong, X. Xu, J.-P. Veder and Z. Shao, *iScience*, 2020, **23**, 100943.

60 Y. Zhong, X. Xu, P. Liu, R. Ran, S. P. Jiang, H. Wu and Z. Shao, *Adv. Energy Mater.*, 2020, **10**, 2002992.

61 X. Wang, J. Sunarso, Q. Lu, Z. Zhou, J. Dai, D. Guan, W. Zhou and Z. Shao, *Adv. Energy Mater.*, 2020, **10**, 1903271.

62 P. Wang, Y. Lin, L. Wan and B. Wang, *ACS Appl. Mater. Interfaces*, 2019, **11**, 37701–37707.

63 J. Qian, X. Bai, S. Xi, W. Xiao, D. Gao and J. Wang, *ACS Appl. Mater. Interfaces*, 2019, **11**, 30865–30871.

64 C. Zhu, Z. Yin, W. Lai, Y. Sun, L. Liu, X. Zhang, Y. Chen and S.-L. Chou, *Adv. Energy Mater.*, 2018, **8**, 1802327.

65 R. Zhao, Q. Li, Z. Chen, V. Jose, X. Jiang, G. Fu, J.-M. Lee and S. Huang, *Carbon*, 2020, **164**, 398–406.

66 P. Zhang, D. Bin, J.-S. Wei, X.-Q. Niu, X.-B. Chen, Y.-Y. Xia and H.-M. Xiong, *ACS Appl. Mater. Interfaces*, 2019, **11**, 14085–14094.

67 Y. Cheng, Y. Wang, Q. Wang, Z. Liao, N. Zhang, Y. Guo and Z. Xiang, *J. Mater. Chem. A*, 2019, **7**, 9831–9836.

68 F. Kong, X. Fan, A. Kong, Z. Zhou, X. Zhang and Y. Shan, *Adv. Funct. Mater.*, 2018, **28**, 1803973.

69 G. Fu, Y. Liu, Y. Chen, Y. Tang, J. B. Goodenough and J.-M. Lee, *Nanoscale*, 2018, **10**, 19937–19944.

70 D. Bin, B. Yang, C. Li, Y. Liu, X. Zhang, Y. Wang and Y. Xia, *ACS Appl. Mater. Interfaces*, 2018, **10**, 26178–26187.

71 Y. Cheng, Y. Guo, N. Zhang, S. Tao, Z. Liao, Y. Wang and Z. Xiang, *Nano Energy*, 2019, **63**, 103897.

72 J. Han, X. Meng, L. Lu, J. Bian, Z. Li and C. Sun, *Adv. Funct. Mater.*, 2019, **29**, 1808872.

This journal is © The Royal Society of Chemistry 2022